Chapter 2

USE OF COMPUTATIONAL THERMODYNAMICS TO IDENTIFY POTENTIAL ALLOY COMPOSITIONS FOR METALLIC GLASS FORMATION

Y. Austin Chang
Dept. of Mat. Sci. and Eng., University of Wisconsin, 1509 University Ave, Madison, WI 53706, USA, chang@engr.wisc.edu

Abstract: A simple thermodynamic analysis illustrates that the formation of a eutectic, e.g. in a binary, is due to the greater thermodynamic stability or the more negative excess Gibbs energy of the liquid versus those of the solid phases. Further decreasing the excess Gibbs energy of the liquid extends its stability to even lower temperatures. Decreases in a liquid's viscosity with concomitant increases in its diffusivity when the temperature is lower, creates a favorable kinetic condition for the formation of materials in the glassy or amorphous state. A calculated isopleth of $Zr_{56.28-c}Ti_cCu_{31.3}Ni_{8.7}Al_{8.5}$, from 0.0 to 15 mol% Ti shows that the liquidus temperature of the quaternary alloy decreases rapidly with the addition of Ti, reaching a minimum at 4.9 mol% Ti, and then increases again. These results indicate that the glass forming ability of the alloys would increase with the addition of Ti, reaching a maximum at or near 4.9 mol% Ti, and then decrease again. This was indeed confirmed experimentally. In a second example, we used a similar thermodynamic analysis to predict alloy compositions of sputter-deposited Al-Zr thin-films in the amorphous state. The predicted alloys compositions were also in accord with those obtained experimentally. In this analysis, we assumed intermetallic compounds do not form due to kinetic constraint since sputter-deposition is an extremely rapid process. In addition we assumed the Gibbs energies of the amorphous phase to be the same as those of the undercooled liquid.

Keywords: phase diagrams, thermodynamics, metallic glasses

1. INTRODUCTION

Bulk metallic glasses (BMGs) exhibit unique properties such as high strength (≈ 300 ksi or 2 GPa), excellent wear and corrosion resistance, high

fracture toughness (50 MPa-$m^{1/2}$), outstanding castability, and low cost for alloy synthesis and fabrication.[1-4] All of these properties make them extremely attractive for practical applications as structural and functional materials. The success in making metallic glasses stimulated from the earlier work of Clement et al. in synthesizing Au-Si glass foils by rapid quenching, 10^5-10^6 K/s, from the melts.[5] Subsequent advances were made with decreasing cooling rates first to 10^3 K/s and eventually to 1 to 10 K/s in the nineteen eighties and nineties.[1,2,6-8] The ability to make these novel metallic materials at cooling rates approaching that of conventional casting conditions affords opportunities not only for investigating the fundamental behavior of deeply undercooled metallic melts but also for manufacturing potential near net-shaped BMG components for practical applications. However, as pointed out by Gottschall,[10] there remains an urgent need to formulate a method for predicting families of alloy compositions with a greater tendency for glass formation. In a recent review, Löffler made the following statement, "-----*the search for new bulk metallic glass compositions is somewhat a 'trial-and-error' method, involving in many cases the production of hundreds to thousands of different alloy compositions*".[11] However, with advancement made in computational thermodynamics, we can indeed calculate multicomponent phase diagrams, from which potential alloy compositions can be identified with tendencies to form BMGs.[12,13] In this chapter, we will first show that the topological features of a simple binary phase diagram are governed by the relative thermodynamic stabilities of the liquid phase versus the competing solid phases. When the liquid phase is much more stable than the solid phases, a eutectic liquid forms. This liquid favors glass formation. We will then next give two examples to demonstrate the success in the use of computational thermodynamics to identify potential alloy compositions for glass formation. While the first example focuses on bulk multicomponent glasses for primarily structural applications, the second one focuses on amorphous binary thin-films as sensors for disk drive applications.

2. PHASE DIAGRAM FEATURES FAVORING GLASS FORMATION

It has been known that the existence of a eutectic in a pseudo-binary oxide system favors glass formation. One example is a soda silicate glass that occurs at the eutectic composition of approximately 76 mol% SiO_2 in Na_2O-SiO_2.[14] The formation of such a eutectic in Na_2O-SiO_2 has its

thermodynamic origin in that the excess Gibbs energy of the liquid phase is more negative than that of the competing solid phases. In the following, we will use a simple regular solution model to represent the excess Gibbs energy of the liquid and solid phases of a simple binary *A-B*. Both *A* and *B* exhibit the same crystal structure such as bcc and their entropies of fusion differ slightly. By varying the regular solution parameters of the solid and liquid phases, different types of phase diagrams can be obtained. The regular solution model is represented by the following equation,

$$G^E = x_A x_B L_0 \tag{1}$$

where G^E is the excess Gibbs energy, x_A and x_B the mole fractions of the component elements and L_0 the regular solution parameter. The Gibbs energy of a phase is,

$$\Delta G = x_A x_B L_0 + RT\left[x_A \ln x_A + x_B \ln x_B\right] \tag{2}$$

where ΔG is the Gibbs energy of a solution relative to those of pure *A* and *B* respectively, *R* the gas constant, and *T* the absolute temperature. The Gibbs energies of fusion of *A* and *B* are,

$$\Delta_{fus} G(A) = 32500 - 11.3T \text{ J mol}^{-1} \tag{3.a}$$

$$\Delta_{fus} G(A) = 38429 - 10.4T \text{ J mol}^{-1} \tag{3.b}$$

In the following, we present three figures with the following sets of solution parameters: Fig. 1.a $L_0(L) = 0$, $L_0(S) = -20$ kJ mol^{-1}, Fig. 1.b $L_0(L) = 0$, $L_0(S) = 20$ kJ mol^{-1}, Fig. 1.c $L_0(L) = 0$ and $L_0(S) = 50$ kJ mol^{-1}; $L_0(L) = -50$ kJ and $L_0(S) = 50$ kJ mol^{-1}. The term one mol means one mole of atoms, i.e. $A_{1-x}B_x$. In all three figures, the solid/liquid phase boundaries (or the solidus/liquidus curves) are also calculated using $L_0(L) = L_0(S) = 0$, i.e. both liquid and solid behave like an ideal solution. The temperatures of the calculated liquidus/solidus curves under this condition, shown as dashed lines, vary monotonically from pure A to pure B. The temperatures of the calculated liquidus/solidus curves using $L_0(L) = 0$ and $L_0(S) = -20$ kJ mol^{-1} shown in Fig. 1.a increase with composition, reaching a maximum and

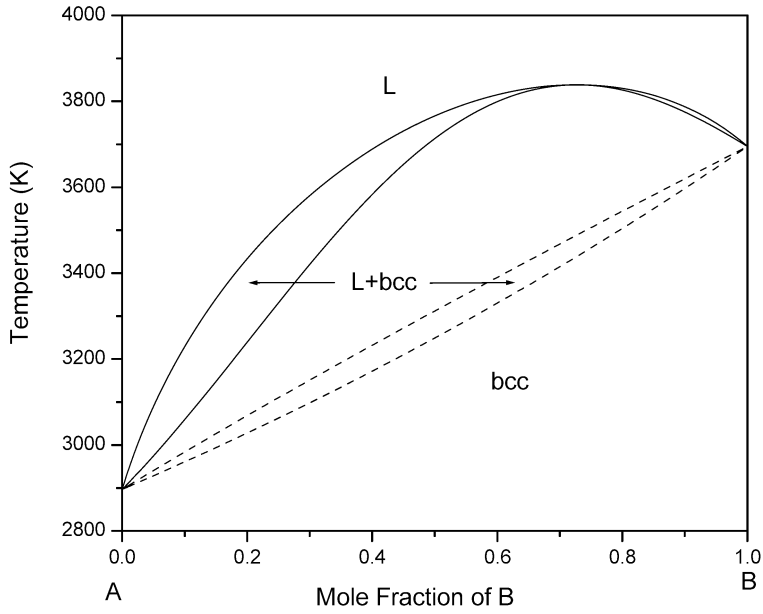

Figure 1.a. Solid lines calculated using $L_0(L) = 0$, $L_0(S) = -20$ kJ mol^{-1}. Dashed lines calculated using $L_0(L) = L_0(S) = 0$.

decrease again. Moreover, the maximum melting temperature occurs at a single composition, i.e. the compositions of the liquid and the solid at the melting point are the same. This kind of melting is referred to as congruent melting. It is similar to the melting of a pure component *A* or *B*. On the other hand, other two-phase alloys melt over a range of temperature with corresponding composition changes. The resulting higher melting temperatures are reasonable since the solid phase becomes thermodynamically more stable with respect to the liquid phase. When both the liquid and solid behave ideally, the liquidus/solidus curves change smoothly with composition. The results shown in Fig. 1.b are the reverse since the regular solution parameter of the solid phase is less exothermic than that of the liquid phase. A minimum congruent melting occurs in this case. In addition to exhibiting minimum congruent melting, something else also happens. The solid phase undergoes phase separation or the formation of a miscibility gap at lower temperatures. According to the regular solution model, the critical point for phase separation is $T_c = L_0(S)/2R = 1203$ K with T_c being the critical point.

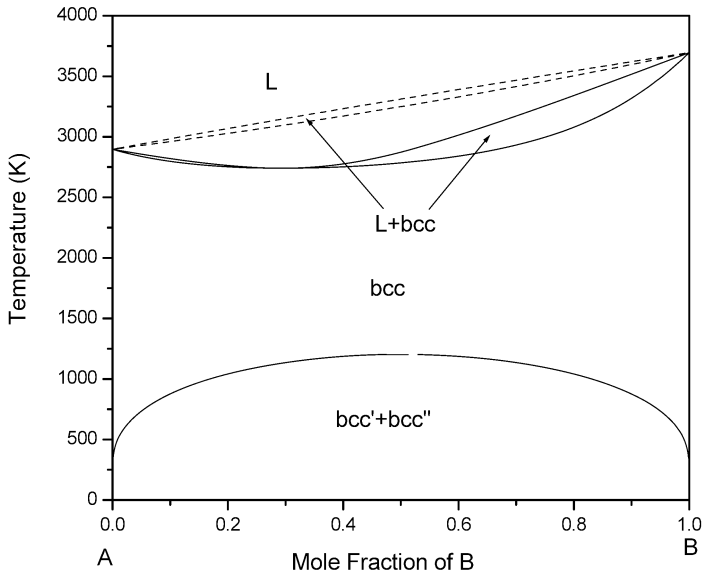

Figure 1.b. Solid lines calculated using $L_0(L) = 0$, $L_0(S) = 20$ kJ mol^{-1}. Dashed lines calculated using $L_0(L) = L_0(S) = 0$.

Figure 1.c shows two calculated phase diagrams. The solid lines are calculated using $L_0(L) = 0$ and $L_0(S) = 50$ kJ mol^{-1}, yielding a eutectic phase diagram. Let us compare the values of $L_0(S)$ used here with that used in calculating the phase diagram in Fig. 1.b since the liquid is ideal in both cases. The thermodynamic parameters indicate that the liquid in this case is much more stable than the solid phase. This condition favors the liquid extending its stability to a lower temperature. When we next increase the value of $L_0(L)$ from 0 to –50 kJ mol^{-1} and keep that of $L_0(S) = 50$ kJ mol^{-1}, the eutectic point is lower by 815 K, frequently referred to as a deep eutectic. This is due to the fact that the liquid becomes even more stable when compared to the solid phase. Binary alloys if indeed exhibiting such a feature would have great tendency to form glass when solidified from the melt at or near the eutectic composition. Since the viscosity of a liquid increases (with a corresponding decrease in diffusivity) when the temperature is lowered, it becomes kinetically favored for this liquid to form glass upon cooling. Moreover, it is known that glasses normally form over a range of composition in the compositional vicinity of the eutectic but requiring larger undercooling at compositions away from the eutectic composition. In the following we will present two examples to show that thermodynamically calculated phase diagrams can indeed predict alloy compositions with great tendencies to form metallic glasses.

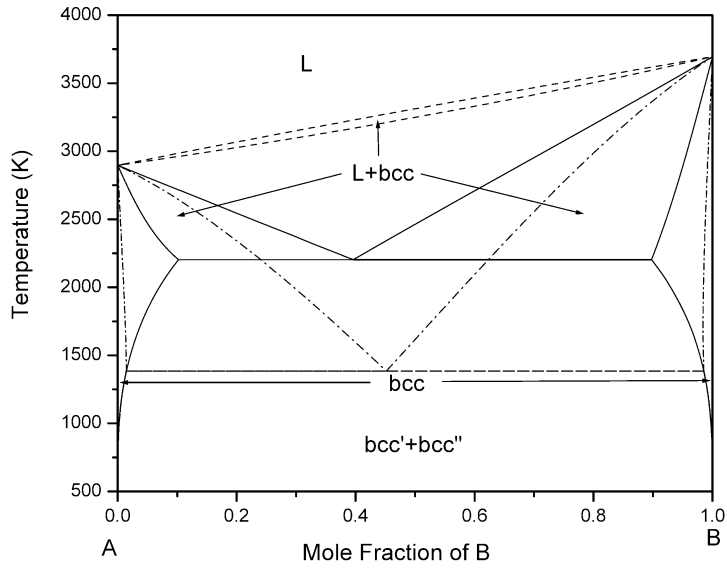

Figure 1.c. Solid lines calculated with $L_0(L) = 0$, $L_0(S) = 50$ kJ mol^{-1} and dashed-dotted line with $L_0(L) = -50$ kJ mol^{-1}, $L_0(S) = 50$ kJ mol^{-1}. Dashed lines calculated using $L_0(L) = L_0(S) = 0$.

However in order to be able to calculate multicomponent phase diagrams, it is necessary to have first a robust phase diagram calculation software, which does not require the supply of initial values by the user. Otherwise the calculation of multicomponent phase diagrams becomes extremely challenging. Often the calculated phase diagrams are not the stable one due to the supply of inappropriate initial values by the users. In addition to the phase diagram calculation software, it is necessary to have secondly thermodynamic descriptions of the multicomponent systems in question.

3. EXAMPLES USING COMPUTATIONAL THERMODYNAMICS TO IDENTIFY ALLOY COMPOSITIONS FOR GLASS FORMATION

3.1 Addition of Ti to improve the glass forming ability (GFA) of a known glass-forming Zr-Cu-Ni-Al alloy

In an attempt to improve the glass forming ability (GFA) of a known quaternary glass-forming alloy, $Zr_{56.28}Cu_{31.3}Ni_{4.0}Al_{8.5}$, Ma et al.[15] recently calculated an isopleth in terms of temperature as a function of the composition of Ti keeping the mol% of Cu, Ni and Al constant at 31.3, 4.0

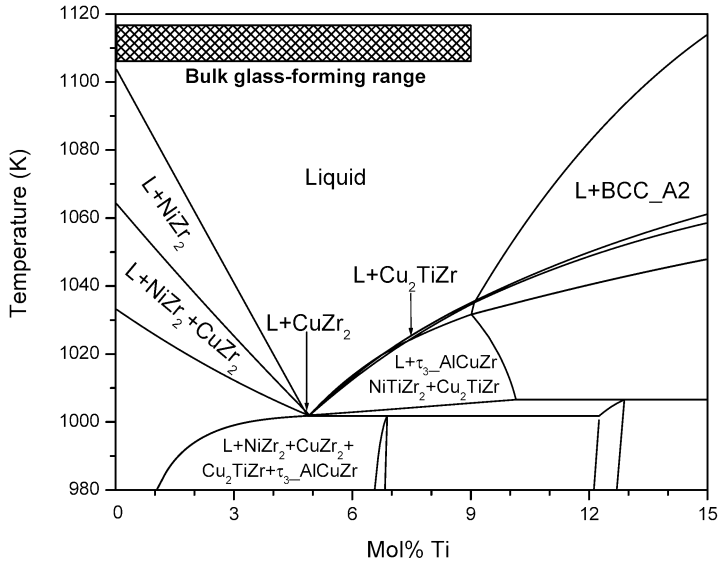

Figure 2. A calculated isopleth, T vs mol% Ti, keeping the mol% of Cu, Ni and Al at 31.3, 4, and 8.5. The alloy composition at the origin is $Zr_{56.2}Cu_{31.3}Ni_{4.0}Al_{8.5}$.

and 8.5 mol%, respectively. Figure 2 shows such a calculated isopleth using the software Pandat.[16-18] It is evident from this figure that the liquidus temperatures from the quaternary alloy $Zr_{56.28}Cu_{31.3}Ni_{4.0}Al_{8.5}$, i.e. without Ti, decrease rapidly reaching a minimum at 4.9 mol% Ti and then increases again. The experimental results obtained by Ma et al. as given below indeed showed that this is the case.[15] A series of $Zr_{56.28-c}Ti_cCu_{31.3}Ni_{8.7}Al_{8.5}$ alloys with values of c varying from 0 to 10 mol% Ti, were prepared with the expectation that the alloy with 4.9 mol% Ti would exhibit the highest GFA. The quaternary $Zr_{56.28}Cu_{31.3}Ni_{4.0}Al_{8.5}$ alloy was found to be a bulk glass-forming alloy based on the calculated low-lying liquidus surface of the quaternary Zr-Cu-Ni-Al system.[19] Alloy ingots with the nominal compositions $Zr_{56.28-c}Ti_cCu_{31.3}Ni_{8.7}Al_{8.5}$ (c = 0 ~ 10.0 mol%) were prepared by arc melting pieces of high purity metals, with Zr being 99.95 wt% and the rest Ti, Cu, Ni and Al being 99.99 wt%, in a Ti-gettered argon atmosphere. Each of the ingot samples was remelted several times to assure good mixing and then suction-cast (or drop-cast), under a purified Ar (or He) atmosphere, into a copper mold with an internal cylindrical cavity with diameters ranging from 1 to 5 mm (or 6 to 14 mm). The amorphous nature of the as-cast rods was examined by analyzing the central part of their cross-sections using X-ray diffraction (XRD) with a Cu-Kα source, and Scanning Electron Microscopy (SEM) in the Backscattered Electron Imaging (BEI) mode. The glass transition and crystallization behaviors of these alloys upon reheating

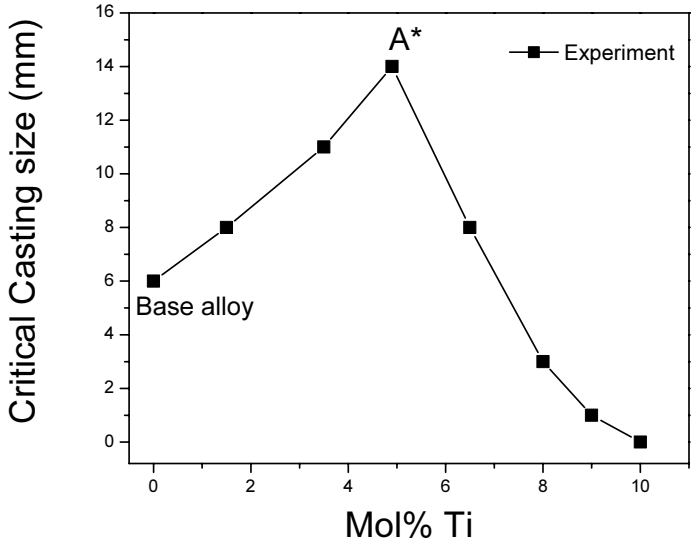

Figure 3.a. Critical diameters of the cast glassy rods vs mol% of Ti. The 14 mm diameter rod at 4.9% is marked A*.

were characterized using a Perkin-Elmer DSC7 (Differential Scanning Calorimeter) at a heating rate of 20 K/min.

As shown in Fig. 3.a the GFA of the quaternary base alloy increases with the addition of Ti in terms of the critical diameters of amorphous rods formed, reaching a maximum at 4.9 mol% Ti and then decrease again. At 10 mol% Ti, it was no longer possible to achieve bulk glass formation. Also shown in Fig. 3.b are the 6 mm-diameter glass rod formed by casting the base alloy and the > 14 mm diameter glass rod formed with the alloy containing 4.9 mol% Ti. Since the technique used by Ma et al.[15] is not capable of casting a rod larger than 14 mm diameter, it was concluded that larger diameters than 14 mm could be obtained. The inset in Fig. 3.b shows an arc-melted 20 gm-button used for casting the amorphous rod of the alloy A*. These results are consistent with the liquidus temperatures shown in Fig. 4. This is anticipated since a minimum amount of undercooling is required at the lowest temperature.

Figure 4 shows the XRD patterns obtained from the as-cast rods of four representative alloys, i.e. $Zr_{56.2-c}Ti_cCu_{31.3}Ni_{4.0}Al_{8.5}$ with c = 0, 1.5, 4.9, 6.5 mol% respectively. They are denoted as the base alloy, A1, A* and A3, respectively. The base alloy exhibits two typical amorphous halos in its 6 mm-diameter sample. On the other hand, the 7 mm-diameter rod shows two crystalline peaks due to the presence of $CuZr_2$ and $NiZr_2$ respectively, indicating that the critical casting diameter for this alloy is ~6 mm.

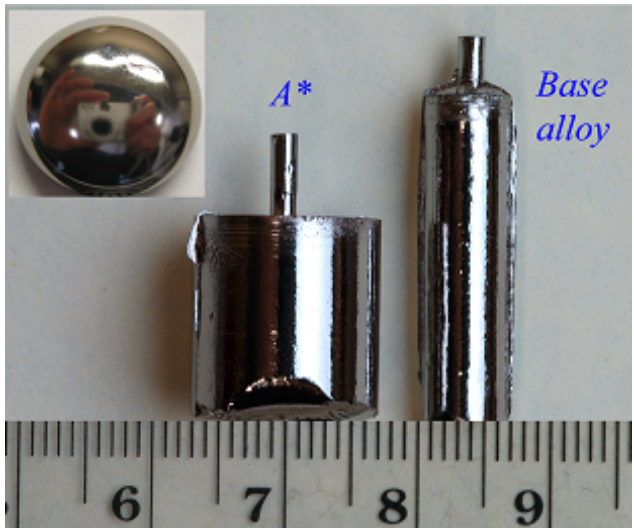

Figure 3.b. Pictures of the 6 and 14 mm diameter glass rods cast from the base alloy and the 4.9 mol% Ti alloy, marked A*. The inset shows an arc-melted 20 gm-button used for casting A*.

The diffraction patterns of the cast 10 mm-diameter rod, from the alloy containing 1.5 mol% Ti and denoted as A1, also exhibit two similar crystalline peaks superimposed on the main halo. These peaks show that this rod is only partially glass. However, it is abundantly clear that there is no crystalline peaks discernible in the XRD patterns of alloy A* obtained from its 5 mm diameter sample. This means that the rod is a monolithic glass. For alloys containing more than 6.5% Ti such as A3, their XRD patterns reveal even more and sharper peaks, indicating the presence of a considerable amount of crystalline phases in their 10 mm-samples. However, with increasing Ti contents beyond this critical composition of 4.9 mol% Ti, the critical casting diameter diminishes rapidly reducing close to nothing when the Ti content reaches 10 mol%.

The DSC curves of the cast amorphous rods presented in Fig. 5 exhibit endothermic inflection characteristic of a glass transition at a temperature, T_g, ranging from 656 to 675 K, followed by one or two pronounced exothermic peaks corresponding to crystallization events. Values of T_x and T_g for each amorphous alloy obtained from the DSC traces with T_x being the onset crystallization temperature are summarized in Table 1. The thermodynamically calculated liquidus temperatures T_l are also given in this table as well as the frequently used GFA criteria, $\Delta T_x = (T_x - T_g)$,[20] T_{rg} [21] and γ.[22] It is found that the value of T_{rg} peaks at 4.9 mol% Ti, which corresponds exactly to the best glass-forming alloy, i.e. A*.

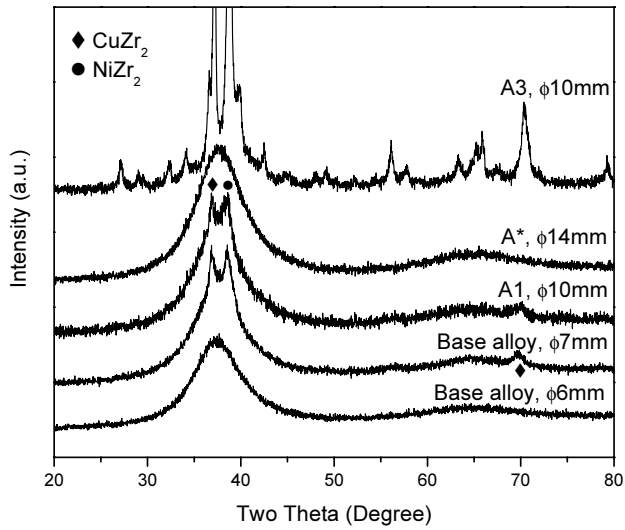

Figure 4. XRD patterns of the 6 and 7 mm dia. rods cast from the base alloy, 10 mm rod from A1 (1.5 mol % Ti), 14 mm rod from A*, and 10 mm from A3 (6.5 mol% Ti).

This is not surprising. Since values of Tg are insensitive to alloy composition, the shape of the compositional dependence of the reduced-glass temperatures is governed by the sharp decreases in the liquidus temperatures. On the other hand, the experimental measured results appear to be somewhat inconsistent with the other two criteria, i.e. ΔT_x and γ.

Except for the above mentioned alloy series (A), Ma et al.[15] also calculated the isopleths in terms of T versus the compositions of Cu, Ni, Al, and ($Zr_{0.5628}Cu_{0.313}Ni_{0.040}Al_{0.085}$) respectively. In other words, each of the elements of Cu, Ni, Al or ($Zr_{0.5628}Cu_{0.313}Ni_{0.040}Al_{0.085}$) was replaced with Ti. First, all the experimentally determined values of the GFA are consistent with the calculated liquidus temperatures. Moreover, the minimum liquidus temperature calculated at 4.9 mol% Ti when replacing Zr is by far the lowest. One can thus conclude that the strategy using the thermodynamically calculated liquidus temperatures has been proven to be robust in locating the bulkiest BMG-former with optimum minor-alloying additions.

3.2 Synthesis of Precursor Amorphous Alloy Thin-films of Oxide Tunnel Barriers Used in Magnetic Tunnel Junctions

We will present in this section how computational thermodynamics can also be used to facility processing innovation for synthesizing precursor

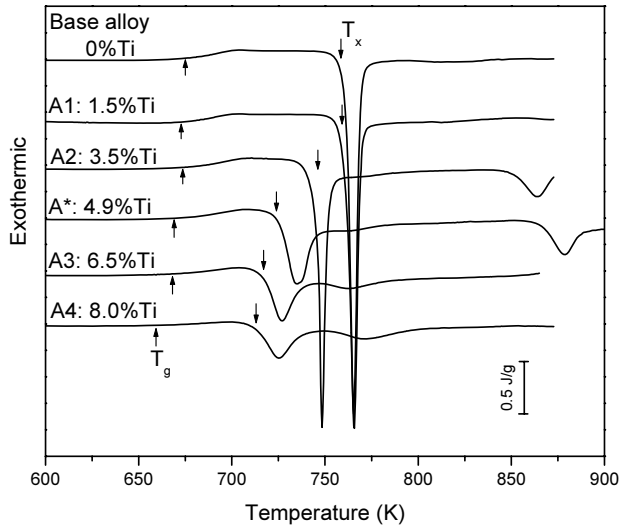

Figure 5. DSC traces of $Zr_{56.2-c}Ti_cCu_{31.3}Ni_{4.0}Al_{8.5}$ alloys (c= 0, 1.5, 3.5, 4.9, 6.5, 8.0) obtained from 2-mm cast rods. The upward arrows indicate T_g and the downward ones T_x.

amorphous alloy thin-films of oxide tunnel barriers used in magnetic tunnel junctions (MTJs). These junctions are being considered as sensitive magnetic sensors and nonvolatile storage cells in magnetic access memories.[23-26] A MTJ consists of two ferromagnetic metal electrodes (e.g. Co) separated by a thin tunnel barrier such as aluminum oxide with a thickness around 1 nm. One of the major challenges is to fabricate MTJs with both high tunneling magnetoresistance (TMR) and low product of junction resistance and area (RA) for practical applications.[27] The quality of a tunnel barrier such as aluminum oxide plays a critical role in the performance of such a device.[28,29] The current practice is to obtain an aluminum oxide barrier by oxidizing a thin crystalline Al layer.[30-34] However, since polycrystalline aluminum films have grain boundaries, the thin oxide barrier formed tends to exhibit non-uniform surfaces as well as other types of defects. An alternative approach is to oxidize an amorphous thin-film of an alloy such as (Al,Zr). The oxide films thus formed tend to exhibit smooth interfaces with fewer defects, thus leading to higher performance of the MTJs, i.e. with greater TMR.[28]

Since an amorphous phase was found in the Al-Zr system with different alloy preparation methods,[35-40] Yang et al.[33] adopted this binary as a model system for their thermodynamic and experimental study.

Table 1. Glass-forming ability and thermal properties of a series of (Zr,Ti,Cu,Ni,Al) alloys (denoted as series A) whose compositions are obtained by replacing Zr with Ti in a base alloy $Zr_{56.2}Cu_{31.3}Ni_{4.0}Al_{8.5}$.

Alloys	Ti Replacement (mol% Ti)	d_{max} (mm)	T_l (K)	T_g (K)	T_x (K)	T_x-T_g (K)	T_g/T_l	$T_x/(T_g+T_l)$
Base alloy	0.0	6	1104	675	761	86	0.611	0.428
A1	1.5	8	1073	673	762	89	0.627	0.436
A2	3.5	11	1030	674	746	72	0.654	0.438
A*	4.9	>14	1002	669	724	55	0.668	0.433
A3	6.5	8	1018	668	717	49	0.656	0.425
A4	8.0	3	1029	659	713	54	0.640	0.422
A5	9.0	1	1035	656	711	55	0.634	0.420
A6	10.0	0	1052	–	–	–	–	–

d_{max}: experimentally attained maximum diameter of glassy rods using copper mould casting.
T_l: the liquidus temperature calculated thermodynamically.
T_g: the glass transition temperature measured using DSC.
T_x: the onset temperature of crystallization measured using DSC.

They presented a thermodynamic formulation to predict alloy compositions, which show tendencies to form amorphous thin-films when fabricated by a rapid quenching process such as sputter-deposition. TEM and XRD were used to confirm the formation of amorphous alloy films. Based on the methodology proposed by Yang et al.,[33] other alloys with higher amorphous-forming ability could be obtained as additional candidates for precursor metals of oxide tunnel barriers.

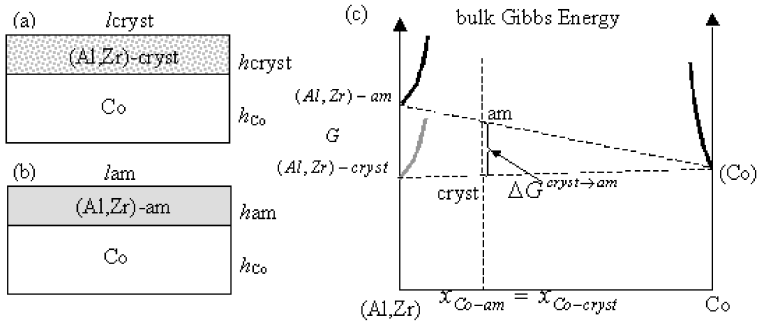

Figure 6. Schematic diagrams of the bilayer structures with the (Al, Zr) layer in (a) crystalline state, (b) amorphous state; (c) the bulk Gibbs energy vs the composition of Co of the bilayer in (a) and (b) for the case that (Al, Zr)-cryst is more stable than (Al, Zr)-am. The symbols l and h refer to the length and height, respectively. The Co layer is in the crystalline state.

Figures 6.a and 6.b show two bi-layered structures, one with an alloy of (Al,Zr) in the crystalline state on top of a thin layer of Co and the other with the same alloy in the amorphous state. The dimensions of the bi-layered structure are given in these figures, i.e. l_{cryst}, l_{am}, h_{am}, and h_{Co}, with the subscripts denoting crystalline and amorphous respectively. The total Gibbs energy of such a bi-layer structure is taken to include three parts: bulk Gibbs energy, interfacial energy and surface energy. The bulk Gibbs energies of these two (Co)/(Al,Zr) bi-layer structures are shown schematically in Fig. 6.c as a function of the Co composition for the structure given in Figs. 6.a and 6.b, respectively. The assumption made is that all the intermetallic compounds normally stable in Al-Zr do not form due to kinetic constraints when using sputter-deposition to fabricate these thin metallic films. In other words, the sputter-deposition process is so rapid that nucleation of these intermetallics becomes unfavorable. In deriving their thermodynamic model, Yang et al.[33] considered only the existence of amorphous and crystalline phases of (Al,Zr). Moreover, the Gibbs energy curves of (Co), (Al, Zr)-am and (Al, Zr)-cryst are represented by sharp curves at the two ends of the diagram because the mutual solubilities between Co and (Al,Zr)-am or (Al,Zr)-cryst are negligible at low temperatures (<500ºC). The tangent line between Co and (Al, Zr)-cryst represents the metastable phase equilibrium between Co and (Al,Zr)-cryst. Similarly, the tangent line between Co and (Al,Zr)-am represents the metastable phase equilibrium between Co and (Al,Zr)-am. The Gibbs energy of the amorphous phase is approximated to be that of the undercooled liquid and the volume Gibbs energies of (Al, Zr)-cryst can be either lower or higher than those of the amorphous phase depending on which state is more stable. Figure 6.c shows the Gibbs energies of a mixture of (Al,Zr)-am and (Co) as well as that of (Al,Zr)-cryst and (Co) as a function of composition of Co at a constant T. For the case shown in this figure, the Gibbs energy of the two-phase mixture consisting of (Al,Zr)-am and (Co) is higher than that of (Al,Zr)-cryst and (Co). At a specific composition of x_{Co}, the Gibbs energy difference between the two states is shown in Fig. 6.c as $\Delta G^{cryst\rightarrow am}$. The symbol $\Delta G^{cryst\rightarrow am}$ denotes the Gibbs energy of transformation from a crystalline state for an (Aly_{Al},Zry_{Zr}) alloy to an amorphous state of an (Aly_{Al},Zry_{Zr}) alloy since (Co) in the structures shown in Fig. 6.a and 6.b remain in the crystalline state. The symbols y_{Al} and y_{Zr} denote the mole fractions of Al and Zr in the binary (Al,Zr) alloys. This transformation energy is the barrier to be overcome for the formation of the amorphous state. The analytical equation of $\Delta G^{cryst\rightarrow am}$ at the as-deposited temperature is described as,[33]

$$\frac{\Delta G^{cryst\rightarrow am}_{(Al,Zr)}}{(1-x_{Co})} = y^{am\,0}_{Al}\Delta H^{fus}_{Al}\left(1-\frac{T_{as}}{T^{cryst}_{m,Al}}\right)+y^{am\,0}_{Zr}\Delta H^{fus}_{Zr}\left(1-\frac{T_{as}}{T^{cryst}_{m,Zr}}\right)$$
$$+\left({}^{ex}G^{am}_{(Al,Zr)}-G^{cryst}_{(Al,Zr)}\right) \quad (4)$$

In Eq. 4, x_{Co} is the overall composition of Co in the bi-layer structure; T_{as} the film deposition temperature; y^{am}_{Al} and y^{am}_{Zr} have been defined above. Since the (1-x_{Co}) term is always positive and does not affect the sign of $\Delta G^{cryst\rightarrow am}$, the Co layer in the model can be replaced by other materials without changing the validity of the conclusions. $T^{cryst}_{m,Al}$ and $T^{cryst}_{m,Zr}$ refer to the transition temperatures from the pure crystalline Al and Zr to their pure liquid, respectively. Similarly, $\Delta H^{cryst\rightarrow am}_{Al}$ and $\Delta H^{cryst\rightarrow am}_{Zr}$ represent the enthalpies of fusion of Al and Zr at their respective melting temperatures. ${}^{ex}G^{am}_{(Al,Zr)}$ and ${}^{ex}G^{cryst}_{(Al,Zr)}$ denote the excess Gibbs energies of the (Al,Zr) alloys exhibiting the amorphous and crystalline state, respectively. In order to evaluate the energy barrier from the (Al,Zr) crystalline to (Al,Zr) amorphous structure, a prerequisite is to know which crystalline structure is the most stable structure. Based on the Gibbs energy of solution phases calculated from the thermodynamic description of the Al-Zr system developed by Wang et al.,[41] the Gibbs energy of the (Al, Zr) solution with the fcc structure was found to be the most stable among the common crystal structures, consistent with the experimental data to be presented later. Using the SGTE lattice stabilities of Al and Zr,[42] and the excess Gibbs energies of the undercooled liquid (Al, Zr)-am and the fcc (Al, Zr)-cryst phases,[41] the values of $\Delta G^{cryst\rightarrow am}$ versus the composition of Zr in the top layer are shown in Figure 7. It is evident from the values of $\Delta G^{cryst\rightarrow am}$ shown in this figure that in the mid-part of the diagram, amorphous alloys are likely to form during sputter-deposition.

It is indeed somewhat surprising that in view of the simplicity of the thermodynamic formulation, the calculated compositions of the (Al,Zr) alloys for amorphous phase formation are in reasonable agreement with the experimental data presented in Figure 8. These data were obtained from TEM micrographs and SAD patterns of co-sputtered deposited alloy films.[33] As shown in this figure, alloys with compositions denoted as A and B exhibit crystal grains with dotted SAD patterns. However, as the composition approaches point C, most of the grains disappear in the micrograph and multiple diffraction rings fade with a halo ring becoming clear in the SAD patterns. This suggests a transitional region from a

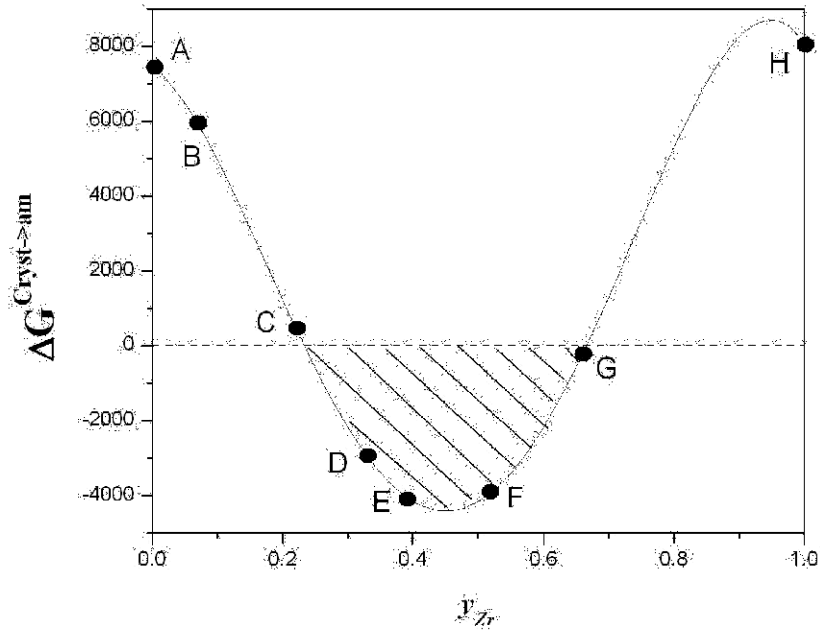

Figure 7. The Gibbs energy difference between the fcc and the amorphous phase of (Al,Zr) vs mol fraction of Zr. Co-sputter deposited films were made at the compositions: A, B, etc. to H.

polycrystalline structure to an amorphous state, in accord with the calculation. With increases in the Zr concentrations, the Al-Zr alloy films appear to be amorphous, which can be seen from the single diffuse ring in SAD patterns and the typical amorphous micrographs[43] (defocused to enhance the contrast) at composition points D, E and F. At point G both the micrograph and the SAD pattern experienced an appreciable change from those of point F, suggesting the film transforms from an amorphous state to a crystalline structure again. At point H, i.e. pure Zr, a polycrystalline fcc structure can be observed from both the micrograph and SAD pattern, indicating the fcc Zr exist. Thicker films with typical compositions were deposited on glass for the XRD structure characterization, as shown in Figure 9. In the three XRD diffraction patterns, the big humps at about 24^{o} result from the glass substrate, which was adopted to exclude any possible peaks from the substrate. This exercise indicates that the thermodynamic approach presented here can be used to make similar predictions for many other alloys and can identify alloy compositions for forming amorphous phases via sputter-deposition, provided thermodynamic descriptions of the alloys in question are available.

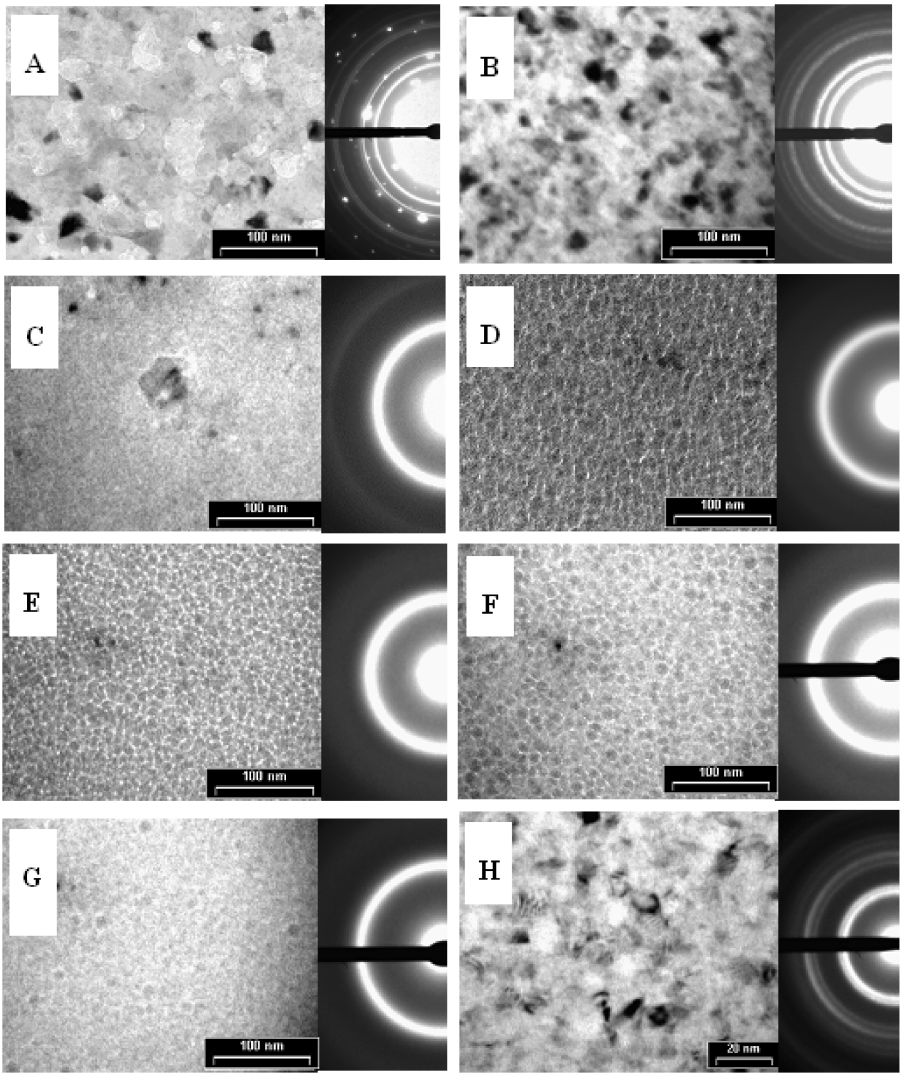

Figure 8. TEM micrographs and SAD patterns of co-sputter deposited (Al, Zr) films at the compositions: A 0, B 7, C 22, D 33, E 39, F 52, G 66, and H 100, all in mol% of Zr.

4. CONCLUSIONS

We have shown that it is possible to use computational thermodynamics to predict alloy compositions with tendencies to form materials in the glassy or amorphous state. Two examples were given. The first one is to add Ti to a known glass-forming quaternary $Zr_{56.28}Cu_{31.3}Ni_{8.7}Al_{8.5}$ alloy in order to

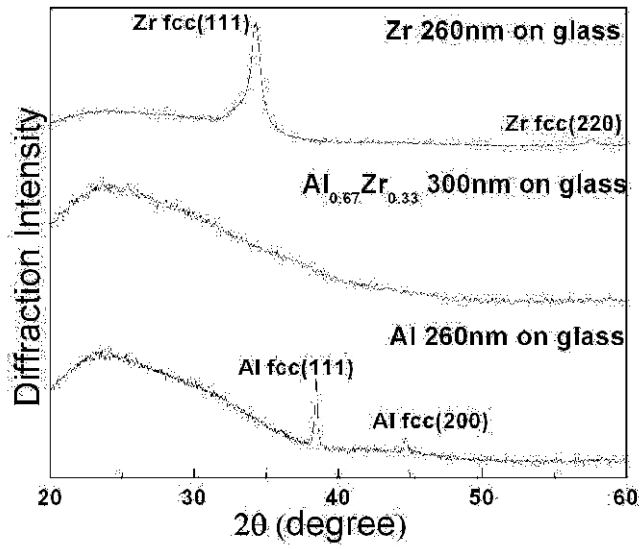

Figure 9. XRD patterns obtained from three typical films on glass: Zr 260 nm, $Al_{0.67}Zr_{0.33}$ 300 nm and Al 260 nm. Note the Zr film exhibits the fcc structure.

improve its glass forming ability. In the second one, we calculated the Gibbs energy difference between the liquid and the fcc phase to predict alloy compositions with tendencies to form amorphous thin-films prepared via sputter-deposition. In both cases, the calculations were confirmedly experimentally.

ACKNOWLEDGEMENTS

I wish to thank my current graduate students, J. Zhu, J. Yang, H. Cao, and C.-H. Ji and my post doc D. Ma, my recent former graduate students Drs. Y. Yang of CompuTherm, LLC, Madison, WI and P. Ladwig of Hutchinson Technology Inc., Hutchinson, MN, for all of their help. The financial support from the DOE-BES (DE-FG-02-99ER45777), the DARPA (ARO Contract No. DAAD 19-01-1-525), and the Wisconsin Distinguished Professorship is gratefully acknowledged.

REFERENCES

1. A. Inoue., High strength bulk amorphous alloys with low critical cooling rates. *Mater. Trans. JIM*, **36**, 866 (1995).
2. W.L. Johnson, Bulk Glass-Forming Metallic Alloys: Science and Technology. MRS Bulletin, **24**, 42 (1999).

3. C.T. Liu, L. Heatherly, D.S. Easton, C.A. Carmichael, J.H. Schneibel, C.H. Chen, J.L. Wright, M.H. Yoo, J.A. Horton, A. Inoue, Test environments and mechanical properties of Zr-base bulk amorphous alloys. *Metall. Mater. Trans*., **29A**, 1811 (1998).
4. R.J. Gottschall, Structure and properties of bulk amorphous alloys: Foreword address, *Metall. Mater. Trans*., **29A**, 1777 (1998).
5. W. Clement Jr., R. H. Willens, and P. Duwez, Noncrystalline structure in solidified gold-silicon alloys, *Nature*, **187**, 869 (1960).
6. H.S. Chen, Thermodynamic considerations on the formation and stability of metallic glasses. *Acta Metall*., **22**, 1505 (1974).
7. A.J. Drehman, A. L. Greer, and D. Turnbull, Bulk formation of a metallic glass: palladium-nickel-phosphorus (Pd40Ni40P20), *Appl. Phys. Lett*. **41**(8), 716 (1982).
8. A. Inoue, T. Zhang, and N. Nishiyama, Preparation of 16 mm diameter rod of amorphous $Zr_{65}Al_{7.5}Ni_{10}Cu_{17.5}$ alloy, *Mater. Trans. JIM*., **34**, 1234 (1993).
9. A. Peker and W. L. Johnson, A highly processable metallic glass: $Zr_{41.2}Ti_{13.8}Cu_{12.5}Ni_{10.0}Be_{22.5}$. *Appl. Phys. Lett.*, **63**, 2342 (1993).
10. R.J. Gottschall, First Conference on Bulk Metallic Glasses, Singapore, 25 October 2000. Sponsored by the United Engineering Foundation, New York, N. Y., USA, 2000.
11. J. F. Löffler, Bulk metallic glasses. *Intermetallic*, **11**, 529 (2003).
12. Y. A. Chang, S.–L. Chen, F. Zhang, X.–Y. Yan, F.–Y. Xie, R. Schmid-Fetzer, and W. A. Oates, Phase Diagram Calculation: Past, Present and Future. *Prog. Mater. Science*, **49**, 313 (2004).
13. Y. A. Chang, Phase Diagram Calculation in Teaching, Research and Industry. *Metall. Mater. Trans*., to be published.
14. F. C. Kracek, The system sodium oxide-silica, *J. Phys. Chem.*, **34**, 1583 (1930).
15. D. Ma, H. Cao, K.–C. Hsieh, L. Ding, Y. Pan, and Y.A. Chang, Bulkier Glass Formation Enhanced by Minor Alloying Additions, Appl. Phys. Lett, under review, 2005.
16. S.–L. Chen, S. Daniel, F. Zhang, Y.A. Chang, W.A. Oates, and R. Schmid-Fetzer, On the Calculation of Multicomponent Stable Phase Diagrams. *J. of Phase Equilb*., **22**, 373 (2001).
17. S.–L. Chen, S. Daniel, F. Zhang, Y.A. Chang, X.–Y. Yan, F.–Y. Xie, R. Schmid- Fetzer, and W.A. Oates, The PANDAT Software Package and its Applications. *CALPHAD*, **26**, 175 (2002).
18. S.–L. Chen, F. Zhang, S. Daniel, F.–X. Xie, X.–Y. Yan, Y.A. Chang, R. Schmid-Fetzer, and W. A. Oates, Calculating Phase diagrams Using PANDAT and PanEngine, *J. of Metal*, **55**, 48 (2003).
19. X.Y. Yan, Y.A. Chang, Y. Yang, F.–Y. Xie, S.–L. Chen, F. Zhang, S. Daniel, and M. H. He, Thermodynamic Approach for Predicting the Tendency of Multicomponent Metallic Alloys for Glass Formation" *Intermetallics*, **9**, 535 (2001).
20. A. Inoue, Stabilization of metallic supercooled liquid and bulk amorphous alloys, *Acta Mater*. **48**, 279 (2000).
21. D. Turnbull, Under what conditions can a glass be formed. *Contemp. Phys*., **10**, 473 (1969).
22. Z. P. Lu and C.T. Liu, Glass formation criterion for various glass-forming systems. *Phys. Rev. Lett.*, **91**, 115505/1 (2003).
23. S.A. Wolf, D.D. Awschalom, R. A. Buhrman, J.M. Daughton, S. von Molnár, M.L. Roukes, A.Y. Chtchelkanova, and D.M. Treger, Spintronics: A spin-based electronics vision for the future. *Science*, **294**, 1488 (2001).
24. J.S. Moodera, L.R. Kinder, T.M. Wong, and R. Meservey, Large magnetoresistance at room temperature in ferromagnetic thin film tunnel junctions. *Phys. Rev. Lett*., **74**, 3273 (1995).

25. I. Zutic, J. Fabian, and S. D. Sarma, Spintronics: Fundamentals and applications. *Rev. Mod. Phys*., **76**, 323 (2004).
26. G. A. Prinz, Magnetoelectronics. *Science*, **282**, 1660 (1998).
27. H. Shim, B.K. Cho, J. Kim, T.W. Kim, and W J. Park, Effect of nitrogen plasma treatment at the Al_2O_3/Fe interface in magnetic tunnel junction. *J. Appl. Phys*., **93**, 7026 (2003).
28. J.S. Moodera, J. Nassar, and G. Mathon, Spin-tunneling in ferromagnetic junctions. *Annu. Rev. Mater. Sci*., **29**, 381 (1999).
29. E.Y. Tsymbal, O.N. Mryasov, and P.R. LeClair, Spin-dependent tunnelling in magnetic tunnel junctions. *J. Phys.: Condens. Matter*, **15**(4), R109 (2003).
30. K. Ohashi, K. Hayashi, K. Nagahara, K. Ishihara, K. Fukami, J. Fujikata, S. Mori, M. Nakada, T. Mitsuzuka, K. Matsuda, H. Mori, A. Kamijo, and H. I. Tsuge, Low-resistance tunnel magnetoresistive head, *IEEE Trans. Magn.*, **36**(5), 2549 (2000).
31. Z.G. Zhang, P.P. Freitas, A.R. Ramos, N.P. Barradas, and J.C. Soares, Resistance decrease in spin tunnel junctions by control of natural oxidation conditions. *Appl Phys Lett.*, **79**, 2219 (2001).
32. J.R. Childress, M.M. Schwickert, R.E. Fontana, M.K. Ho, P.M. Rice, and B.A. Gurney, Low-resistance IrMn and PtMn tunnel valves for recording head applications., *J. Appl. Phys*., **89**, 7353 (2001).
33. J.J. Yang, P.F. Ladwig, Y. Yang, C.–X. Ji, F.X. Liu, B.B. Pant, A.E. Schultz, and Y.A. Chang, Oxidation of tunnel barrier metals in magnetic tunnel junctions. *J. Appl. Phys*., in press, 2005; J.J. Yang and Y.A. Chang, Amorphous alloy thin films as precursor metals of oxide tunnel barrier used in magnetic tunnel junctions. *J. Appl Phys*., in press, 2005.
34. P.F. Ladwig, J.J. Yang, Y. Yang, F. Liu, B.B. Pant, A.E. Schultz, and Y.A. Chang, Selective Oxidation of Tunnel Barrier Metals in Magnetic Tunnel Junctions. *Appl. Phys. Lett*., in press, 2005.
35. S. Lee, C. Choi, and Y. Kim, Effect of Zr concentration on the microstructure of Al and the magnetoresistance properties of the magnetic tunnel junction with a Zr-alloyed Al–oxide barrier. *Appl. Phys. Lett*., **83**, 317 (2003).
36. E. Ma, and M. Atzmon, Calorimetric evidence for polymorphous constraints on metastable zirconium-aluminum phase formation by mechanical alloying. *Phys. Rev. Lett*, **67**(9), 1126 (1991).
37. E. Ma, F. Brunner, and M. Atzmon, Stability and thermodynamic properties of supersaturated solid solution and amorphous phase formed by ball milling in the zirconium-aluminum system. *J. Phase Equil.*, **14**(2), 137 (1993).
38. H.J. Fecht, G. Han, Z. Fu, and W.L. Johnson, Metastable phase formation in the zirconium-aluminum binary system induced by mechanical alloying, *J. Appl. Phys*., **67**, 1744 (1990).
39. H. Yoshioka, H. Habazaki, A. Kawashima, K. Asami, and K. Hashimoto, Anodic polarization behavior of sputter-deposited aluminum-zirconium alloys in a neutral chloride-containing buffer solution. *Electrochimica Acta,* **36**, 1227 (1991).
40. J. Ho and K. Lin, The metastable Al-Zr alloy thin films prepared by alternate sputtering deposition. *J. Appl. Phys*., **75**, 2434 (1994).
41. T. Wang, Z. Jin, and J C. Zhao, Thermodynamic assessment of the Al-Zr binary system. *J Phase Equil*., **22**, 544 (2001).
42. A.T. Dinsdale, SGTE data for pure elements, *CALPHAD*, **15**, 317 (1991).
43. D. Williams, and C.B. Carter, *Transmission Electron Microscopy: A Textbook for Materials Science*, Chapt. 28, Plenum Press, New York, 1996.

http://www.springer.com/978-0-387-23117-4

Applied Computational Materials Modeling
Theory, Simulation and Experiment
Bozzolo, G.; Noebe, R.D.; Abel, P.B. (Eds.)
2007, XVI, 491 p., Hardcover
ISBN: 978-0-387-23117-4